

Internal tides generated on a corrugated continental slope:
Part 1: Cross-slope barotropic forcing

Sonya Legg

Department of Physical Oceanography,
Woods Hole Oceanographic Institution, Woods Hole, MA 02543
Submitted to Journal of Physical Oceanography

May 14, 2003

Abstract

Recent measurements in a region of continental slope characterised by ridges and valleys running up and down the slope reveal interesting high-mode structure in the tidal band velocity signals, and enhanced mixing over the corrugations. In order to deduce the processes responsible for the observed phenomena we have performed numerical simulations of the internal tide generation in this region of topography. Here we focus on the response of the flow to cross-slope barotropic tidal forcing. The flow response is characterised by an internal tide generated at the shelf break which subsequently reflects from the corrugated slope. Above the corrugated slope, we find that high-mode structure may be created, but only if the Coriolis force is included. We propose interference between the primary internal tide, and secondary internal waves forced by the Coriolis driven along-slope component of primary wave flow field as the cause of the high-mode structure in the simulations. Under suitable conditions of forcing, topography and stratification, the shear generated by the interference may lead to local mixing. Hence complex topography may be an important contributor to boundary mixing in the ocean.

1 Introduction

The barotropic tide, when it encounters topographic variations in a density-stratified fluid, can lead to both local mixing and generation of internal waves at the tidal frequency (internal tides). Munk and Wunsch (1998) have highlighted the importance of the conversion of barotropic-to-baroclinic tidal energy, and the subsequent conversion of baroclinic energy to turbulent motions, in the maintenance of the meridional overturning circulation through diapycnal mixing. Recent observations (Polzin et al. 1997, Ledwell et al. 2000 and St. Laurent et al. 2001) have shown that while diapycnal mixing is small over much of the ocean interior, in regions of rough topography mixing is large and correlated with the fortnightly tidal modulation in the bottom-most 1-2 km. This emphasizes the importance of the tides. But given the impossibility of directly measuring diapycnal mixing throughout the world ocean, better understanding of the phenomena is required in order to represent the effects of tidally produced diapycnal mixing in general circulation models.

Numerical simulations are used here to examine the conversion of barotropic-to-baroclinic energy and diapycnal mixing. The physical parameters are taken to be representative of the Mid-Atlantic Bight just north of Cape Hatteras. This region was the subject of a recent field program described in Nash et al (2002) and referred to hereafter as TWIST (Turbulence and Waves over Irregularly Sloping Topography). This study region is particularly interesting because it contains two-dimensional topographic variations (corrugations) running up and down the slope (figure 1a). The slope itself is supercritical (i.e. the topographic slope exceeds the the slope of the tidal characteristic) near the shelf break, and less steep at depth (a concave slope). The stratification is highly nonuniform, with much stronger stratification near the surface than at depth (figure 1b).

These features contrast with many assumptions made by existing studies of the baroclinic/barotropic energy conversion process, e.g. small-amplitude topography, linear 1-dimensional slopes and uniform stratification.

Nonetheless, earlier theoretical studies of the generation of internal waves by barotropic flow

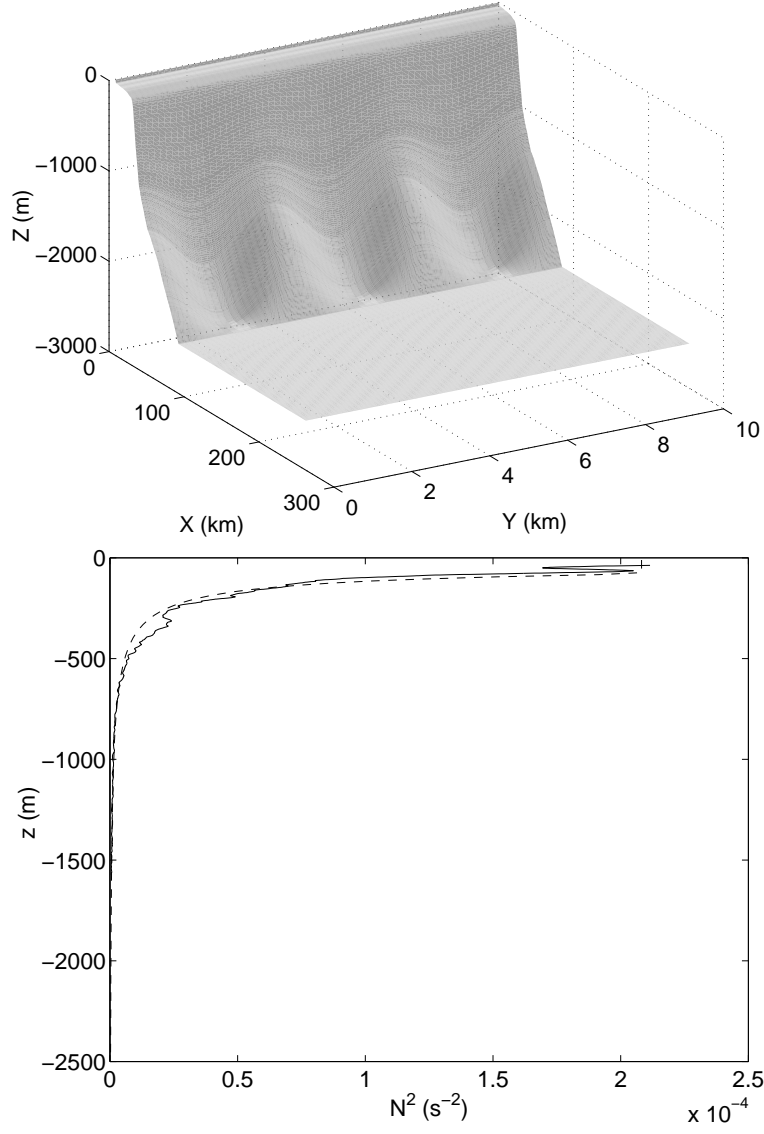


Figure 1: (a) The topography used in the model. The mean slope is an alongslope average of the actual topography of the TWIST region. Sinusoidal along-slope variations are superimposed on this mean slope, with a wavelength of $10/3$ km. (b) The stratification $N^2 = (g/\rho_0)d\rho/dz$, as a function of depth, from the observations (solid line) and a monotonic best fit powerlaw profile of the form $N^2 = 1.1007(-z)^{-1.9564}$ for $z < -80$ m, and $N^2 = 1.1007 \times 80^{-1.9564}$ for $z > -80$ m.

over topography do provide important guidance to our numerical study. First they focus attention on the governing nondimensional parameters. The governing parameters of our problem are (a) U_0 , the barotropic tidal forcing amplitude (b) ω_0 , the tidal frequency, (c) N , the buoyancy frequency, (d) f , the Coriolis frequency, (e) H , the total depth of the fluid, (f) dh/dx the slope of the topography, (g) h , the height of the topography, or L , the horizontal lengthscale of the topography. An important non-dimensional combination of N , ω_0 and f is the slope of an internal wave group velocity characteristic

$$s = \frac{\partial\omega}{\partial m} / \frac{\partial\omega}{\partial k} = \frac{k}{m} = \left(\frac{\omega_0^2 - f^2}{N^2 - \omega_0^2} \right)^{1/2} \quad (1)$$

(where k is the horizontal wavenumber and m is the vertical wave number of the internal wave at frequency ω_0), and especially the ratio between the topographic slope and the wave slope

$$\frac{dh/dx}{s} = \epsilon = \text{Topographic steepness} \quad (2)$$

When $\epsilon > 1$, the slope is said to be supercritical, when $\epsilon < 1$, the slope is subcritical and when $\epsilon = 1$ the slope is critical. Early work (e.g. Cox and Sandstrom 1962, Rattray 1960, Baines 1982) focused upon the issue of finite amplitude bathymetry, i.e. ($\epsilon \neq 0$), with the former formulating the problem in terms of a power series expansion of the bottom boundary condition and the later adopting a streamfunction representation. The streamfunction approach highlights the issue of beams of internal tide energy emanating from critical points. This is easily understood in geometric terms, as the critical point marks a transition from energy propagating outward from a steep slope in both vertical directions to propagation upward from a subcritical slope in both horizontal directions. Rattray emphasizes that such rays are also regions of high shear and possible locations of heightened mixing. The approaches detailed in Rattray-Baines are not limited to small slopes, and hence are particularly useful for estimating internal tide generation from continental shelf regions, where order(1) changes in depth occur. However, they are limited to problems involving one-dimensional topography. Thus they cannot effectively address the impact of small-scale irregularities superimposed upon the continental slope.

Whether fluid advection can be assumed negligible is also important for mixing. This assumption can be characterized as assuming $R_L \ll 1$, where

$$R_L = \frac{U_0}{\omega_0 L} = \frac{\text{Tidal excursion distance}}{\text{Horizontal topographic lengthscale}} \quad (3)$$

Bell (1975) does not assume $R_L \ll 1$, but does assume $\epsilon \ll 1$ everywhere, i.e. small amplitude topography. Bell demonstrates that, in the advective limit ($R_L \gg 1$), the response is similar to the generation of internal waves by a steady flow over topography. In particular, internal waves with an intrinsic frequency higher than tidal are generated. The internal wave amplitude is relatively smaller for topographic scales in the advective limit. Incorporation of tidal advection represents, effectively, a smoothing operation.

Analytic progress in the case of finite topographic steepness and tidal excursion is difficult. Recent theoretical work (Balmforth et al, 2002, St Laurent and Garrett, 2002) has extended Bell's

predictions into the regime $\epsilon \rightarrow 1$, for small R_L , and found a relatively small enhancement of internal tide energy flux for steep topography. In numerical simulations Khatiwala (2002) shows that for certain topographies, the energy flux can saturate for $\epsilon > 1$. St Laurent et al (2003) examine the limit of $\epsilon \rightarrow \infty$, small R_L for knife-edge ridges, and vertical continental slopes. Polzin (2002) demonstrates that both finite amplitude bathymetry and tidal advection are important for determining the internal wave shear and distribution of mixing associated with internal wave breaking. Ultimately progress in the regime of large ϵ , large R_L can only be made with fully nonlinear numerical models. Several recent examples of primitive equation modeling of internal tides with realistic 3-dimensional topography include Holloway (2001), Merrifield and Holloway (2002). Here we examine both the internal tide generation, and the conditions which may lead to tidal mixing on a corrugated slope, using a nonhydrostatic model.

Here generation of internal tides at the shelf break and their subsequent reflection and scattering from the continental slope and rise are examined. This and similar situations have been studied before in linear ($R_L \ll 1$) models with infinitesimal amplitude topographic perturbations on an infinite planar slope (Thorpe 1992, 1996 and 2001) or one-dimensional topographic planforms Müller and Liu 2000a,b. Thorpe 2001 considers a scenario of particular relevance to the TWIST region - the reflection and scatter of internal waves from a slope with regular corrugations. That study, however, neglects rotation and assumes small ϵ and small R_L .

The TWIST region has large-amplitude topography. On the shelf the slope is subcritical, below the shelf it is supercritical, and further down it is again subcritical. There are thus two locations of critical slope in the cross-slope direction, one at the shelf break and one halfway down the slope. In practise an internal tide beam emanates only from the critical point where the slope is convex (i.e. the shelf-break) (at the concave critical slope at mid-depths topography prevents fluid parcels from moving along the characteristics, the direction of fluid motion in a propagating internal wave, Gilbert and Garrett (???)). The forcing generating the internal wave is also greatest at the shelf break, where shallow fluid is combined with large slope curvature (Baines, 1982).

A wave generated at the shelf break, propagating offshore along its characteristic, will reflect from the topography in the region of subcritical slope, preserving the angle of propagation with the horizontal. The focus of this paper is the role of a corrugated slope in internal wave reflections.

We are motivated in our study by several interesting features of the observations in the TWIST region (Nash et al, 2002). First, diapycnal mixing is observed close to the bottom, over the corrugations. Diffusivities are considerably smaller at the shelf-break where one might expect the barotropic currents to be much stronger. Secondly, the baroclinic currents show interesting vertical structure, with several zero crossings in the vertical, suggesting a modal character, with high vertical wavenumber (and small vertical wavelength).

The observations in the TWIST region spanned many different time-scales, including subinertial flow and possible topographic waves. However, here we will confine ourselves to the baroclinic response to the tidal forcing, ignoring lower-frequency flows. Comparison between the observations and model results is particularly useful for demonstrating the inadequacy of some model assumptions (e.g. 2-dimensional topography) and stimulating the inclusion of greater complexity into the numerical simulations. In order to fully identify the range of physical processes which may occur in tidal-continental slope interactions, our simulations cover a wider range of parameter space than

found in the observations, and explore more extreme limits. Our results may therefore be applicable to a wide range of continental slope conditions, not just the TWIST study region.

In this study we focus on the features associated with the internal tide generated locally by the barotropic tidal flow over the continental slope topography. In our comparison with observations we examine whether these processes can account for the observed velocity structure and mixing. There are of course other alternative explanations for tidal frequency baroclinic velocities - for example remotely generated internal tides. That possibility is examined in detail in Nash et al (2003).

2 Model formulation

To examine the interaction between tides and the complicated topography of the TWIST region, we use the MIT Ocean model (Marshall et al, 1997). This model is well suited for this problem because it includes: (a) arbitrary topography, through the use of a finite volume formulation (Adcroft et al, 1997); (b) full nonhydrostatic physics, allowing mixing features such as internal hydraulic jumps and Kelvin-Helmholtz instability to be explicitly simulated, and removing the need for a parameterization of these mixing processes; (c) a free-surface formulation, allowing the barotropic tide to be satisfactorily represented; (d) efficient parallelization, allowing the model to be run at sufficiently high resolutions to resolve the mixing processes described above. The model domain is shown schematically in figure (1a). The x-direction is cross-slope, and the y-direction is along-slope. The model allows for variable resolution in all directions, and we make use of this to focus resolution on the slope, with coarser resolution offshore. The domain size for most calculations is $L_x \times L_y \times H = 254km \times 10km \times 2505m$, and the resolution is $nx \times ny \times nz = 328 \times 60 \times 64$. The variable grid size in the x-direction is such that over the slope $\Delta x = 370m$, coarsening to close to 2km near the offshore boundary. The vertical grid spacing is $\Delta z = 10m$ in the strongly stratified thermocline, coarsening to $\Delta z = 73m$ at depth. Some of our calculations have additionally enhanced resolution. The resolution in the along-slope direction is $\Delta y = 156m$ in most calculations. Three wavelengths of the corrugated topography are included in the domain. We also investigate the effect of variable corrugation wavelength, and for those calculations use a different L_y , retaining 3 wavelengths in the domain, keeping $ny = 64$, and changing Δy accordingly. Horizontal diffusivity and viscosity are $10^{-1}m/s^2$, and vertical diffusivity and viscosity are $10^{-2}m/s^2$. These rather large values are required in order to prevent grid-scale noise from appearing, given the relatively coarse resolutions. These values are certainly higher than the background levels of turbulent diffusivity measured in the ocean ($\kappa_v \approx 10^{-5}m^2s^{-1}$) and therefore simulations at these coarse resolutions cannot provide quantitative estimates of the diffusivities associated with diapycnal mixing. Rather the aim here is to examine the processes which lead to small Richardson numbers.

The initial density field is horizontally uniform, with a vertical stratification which is a powerlaw best-fit to the observed density field. (Density is a linear function of temperature only - we ignore salinity in these calculations). The topography consists of the along-slope average topography taken from observations, with sinusoidal corrugations superimposed. We begin with the simplest scenario - 2-dimensional topography, and gradually increase the complexity, in order to identify those factors which control the observed tidal frequency current variability, and perhaps the resultant mixing.

The cross-slope barotropic tidal forcing is applied through a specified flow at the offshore boundary, $x = L_x$:

$$u = U_0 \sin(\omega t), v = 0, w = 0, T = T_i(z) \quad (4)$$

where $T_i(z)$ is the initial temperature profile. These boundary conditions do not allow waves to propagate out of the domain, and so L_x has been chosen sufficiently large to allow several tidal cycles of calculation before internal tides reach the offshore boundary (where they will reflect and contaminate the solution). The vertically uniform barotropic current oscillates at the M2 tidal frequency $\omega = 1.41 \times 10^{-4} s^{-1}$. The amplitude of the barotropic tide at the boundary where forcing is applied is $U_0 = 0.1 m/s$ in most of the calculations described (this is larger than observed, so we include comparison with smaller amplitude forcing, as well as exploring the response to more extreme forcing). The barotropic currents increase toward the shelf-break, to satisfy mass continuity as the topography approaches its shallowest depth. $U_0 = 0.1 m/s$ corresponds to $R_L = 0.01$, where the distance between shelfbreak and the bottom of the slope has been used for the topographic lengthscale. For such small R_L the response is expected (according to Bell, 1975) to be dominated by the forcing frequency. Elsewhere boundary conditions are no flow at the onshore boundary, noslip at the topographic boundary and periodic in the along-slope direction.

3 Results

3.1 2-dimensional calculations

Our first calculations have no along-slope topographic variations, and hence 2-dimensional calculations (allowing flow in the along-slope direction, but no y-variations in any quantities) are sufficient. The topographic slope is critical at the shelf-break, and in accordance with predictions by Rattray (1960) and Baines (1982), internal wave beams emanate from this critical point. Energy initially propagates along a narrow beam which closely follows the internal wave characteristic emanating from the shelf-break (figure 2). The characteristic intersects the subcritical bottomslope. Upon reflection, the internal wave acquires a more modal character (that is to say that particular depths are nodes while others are locations of maximum flow variability (or antinodes)). with the lowest mode dominating (i.e. one node). This low mode structure might result from dissipation of the higher modes, or combination with a beam reflected from the surface. The mode-one internal wave, with velocity maxima near the surface and the bottom, propagates offshore. Note that the mode one internal wave has no shear near the bottom (apart from a poorly resolved bottom boundary layer in the bottom grid cell). This internal wave structure contrasts with the observed high-mode structure and the observed maxima in dissipation near the bottom. Without shear, there is no possibility for shear-generated mixing. In addition there is little flow at all in the shadow zone below the wave characteristic.

3.2 3-dimensional calculations

The structure of the observed currents clearly cannot be explained by the simplistic 2D scenario. We now examine the response to barotropic flow over 3-dimensional topography containing corrugations.

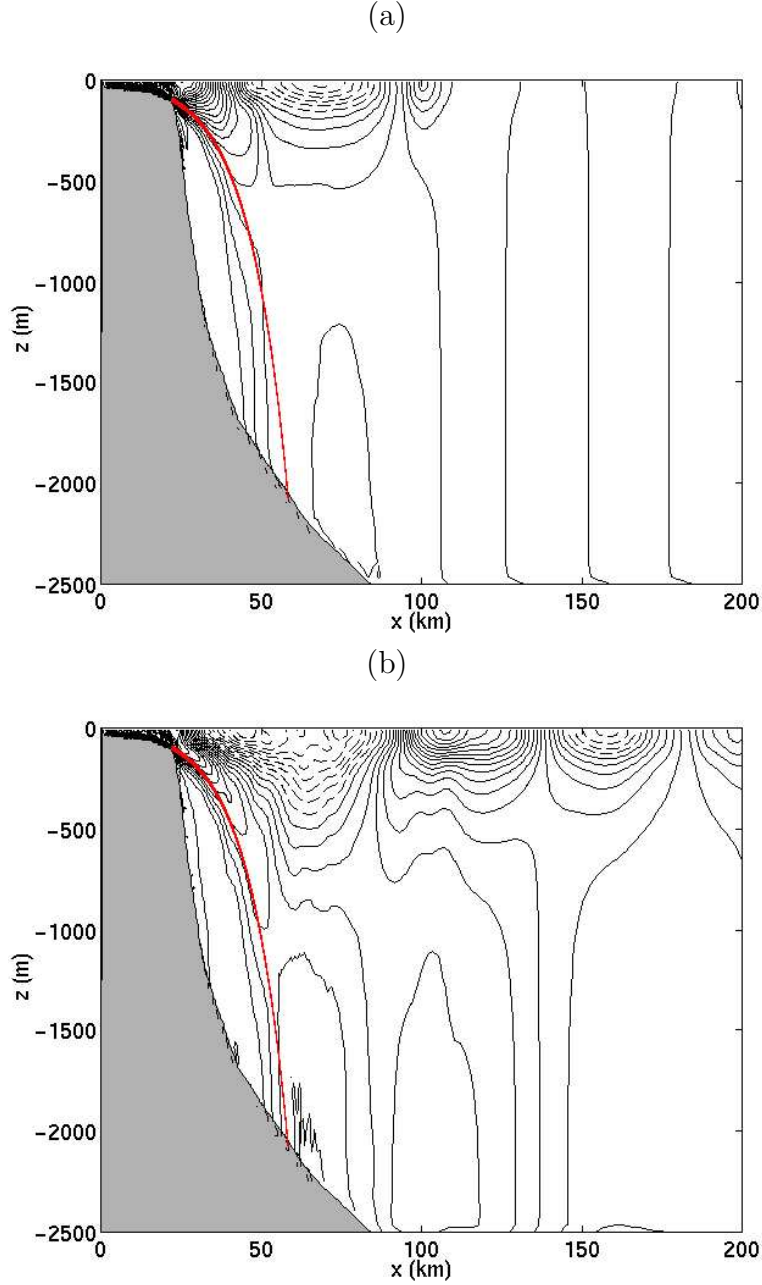


Figure 2: The cross-slope currents generated by interaction between the barotropic tide and the 2-dimensional continental slope topography, at times $1.2T$ and $3.1T$ after the beginning of the forcing, where T is the tidal period of 44567s. The contour spacing is 0.01m/s. Solid lines indicate offshore currents, dashed lines indicate onshore currents. The red line indicates the characteristic of the internal wave at the tidal frequency emanating from the shelf-break.

The topography is of the form

$$h(x, y) = h_0(x) + h_a \sin(2\pi y/\lambda_y + \pi/2.0) \sin(\pi \left(\frac{x - x_d}{x_s - x_d} \right)) \text{ for } x_s < x < x_d \quad (5)$$

$$h(x, y) = h_0(x) \text{ for } x < x_s \text{ and } x > x_d \quad (6)$$

where $h_0(x)$ is the topographic depth previously used in the 2D calculations (the along-slope average of the actual topography from the TWIST region), λ_y is the wavelength of the topographic corrugations ($10/3km$), x_d is the cross-slope coordinate of the foot of the slope (i.e. where $h_0(x) = \text{maximum depth}$), and x_s is the cross-slope coordinate of the shelf break: $x_s = 22.5km$ and $x_d = 84.6km$. h_a is the amplitude of the corrugations: $h_a = 300m$. This topography specification ensures that the shelf-break remains invariant in the y-direction, and the corrugations have their maximum amplitude halfway along the slope. While we selected the wavelength of the topography to match the dominant wavelength of the observations, the wavelength of the corrugations increases with depth in the actual observed topography. Hence by 2000m depth the model corrugations are too small in wavelength and too large in amplitude compared to the actual topography. However, we address this by exploring the sensitivity to corrugation wavelength in a later section.

Figure 3 shows the cross-slope velocity in a valley at the same instants as in figure 2. Now there is significant shear in the valley bottom at $x = 50 - 80km$. At the later time, much more structure has developed in the velocity field on smaller vertical scales. Cross-sections of the cross-slope velocity through the corrugated topography at $x = 58.7km$ show that this small-scale structure is organized above the valleys and shows a y-wavenumber governed by that of the topography (figure 4). (Asymmetries about the center of the valleys are temporal - at a different phase of the tide, structures would be located on the opposite side of the valley).

This small-scale structure is perhaps more easy to visualize by looking at profiles of the baroclinic component of U as a function of z and time, shown for $x = 58.4km$ and $y = 1.56km$ (figure 5). For comparison similar profiles are shown from calculations without corrugations and without planetary rotation. The 2D rotating case shows a mode 1 structure, with a node at about 800m depth, where baroclinic velocities are always small, and velocity maxima near the top and bottom of the water column. The 2D nonrotating case shows a similar structure, although the first mode structure appears to develop somewhat further from the topography, so there is still some vertical phase propagation near the surface at this location. (The location is slightly downstream of the first reflection from the topography, since the characteristic intersects the slope slightly higher up for the nonrotating case). The 3-D rotating profile shows quite a different structure: the structure near the surface seems approximately unchanged, but below 800m, several more nodes of minimum variability (although not regions of zero variability) appear. By contrast the 3D nonrotating profiles differ little from the 2D nonrotating profiles. That the nonrotating and rotating runs differ so strongly implicates rotation in the generation of this structure on smaller vertical scales. A significant difference between the nonrotating and rotating internal tide is that the rotating internal tide includes along-slope velocity, with an amplitude $V_a = U_a f/\omega$ where U_a is the amplitude of the cross-slope internal tide velocity. This finite along-slope velocity allows the internal tide to interact with the along-slope corrugations when the internal tide encounters the topography.

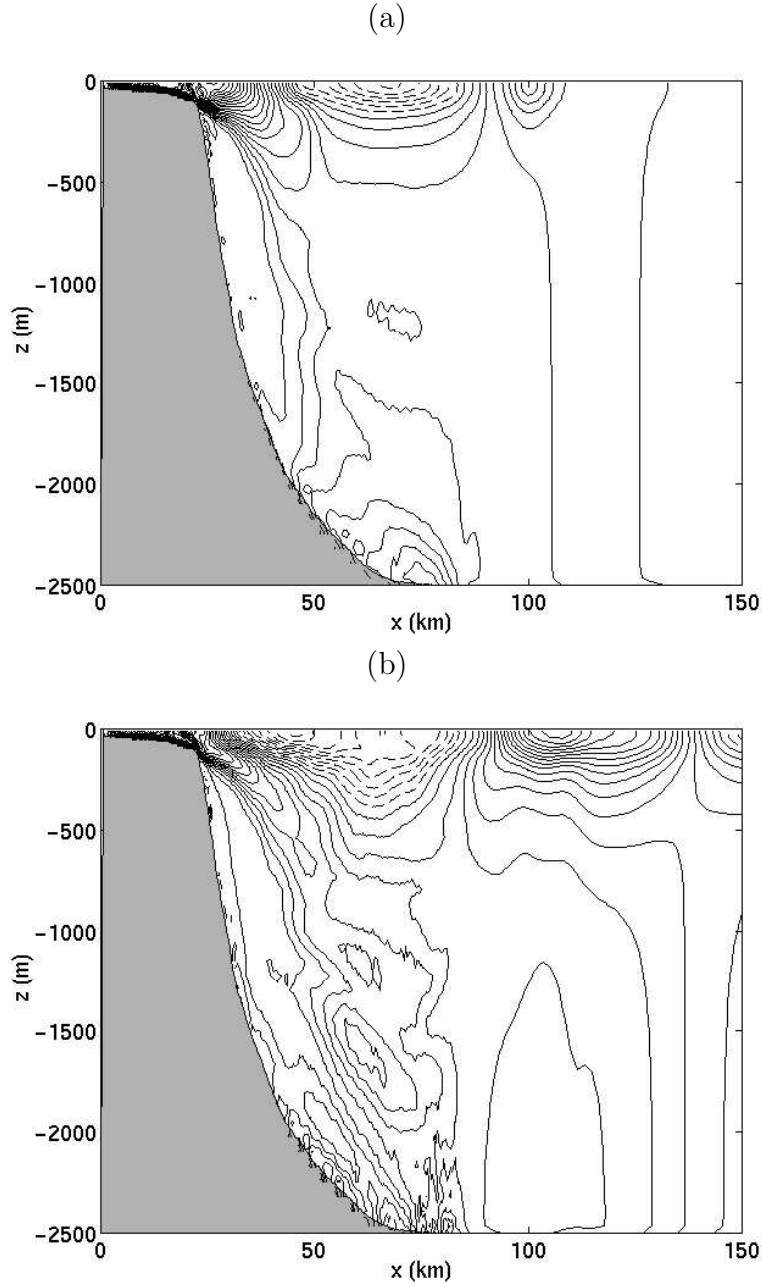


Figure 3: The cross-slope currents generated by interaction between the barotropic tide and the 3-dimensional continental slope topography, shown in a canyon region ($y = 1.56km$) at times $1.2T$ and $3.1T$ after the beginning of the forcing, where T is the tidal period of $44567s$. The contour spacing is $0.01m/s$. Solid lines indicate offshore currents, dashed lines indicate onshore currents.

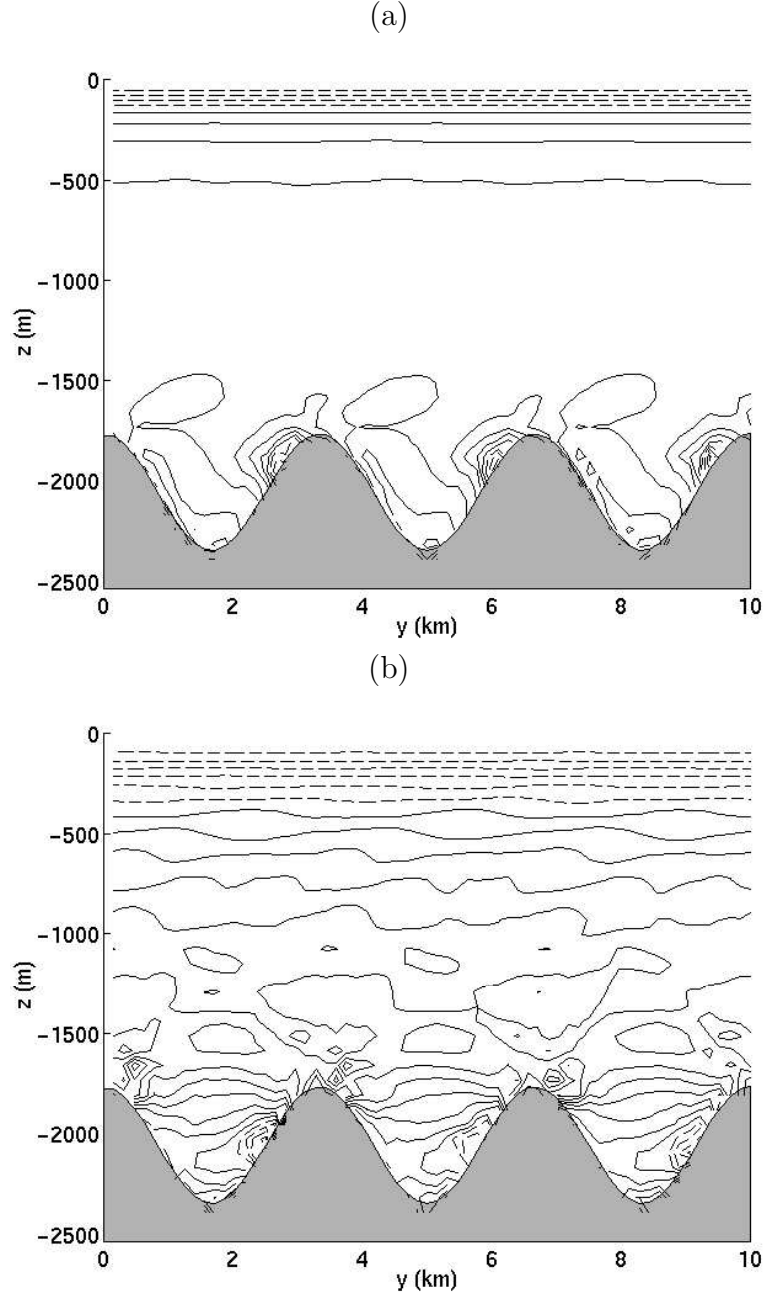


Figure 4: The cross-slope currents generated by interaction between the barotropic tide and the 3-dimensional continental slope topography, shown as a function of y and z at a location $x = 58.7\text{km}$, at times $1.2T$ and $3.1T$ after the beginning of the forcing, where T is the tidal period of 44567s . The contour spacing is 0.01m/s . Solid lines indicate offshore currents, dashed lines indicate onshore currents.

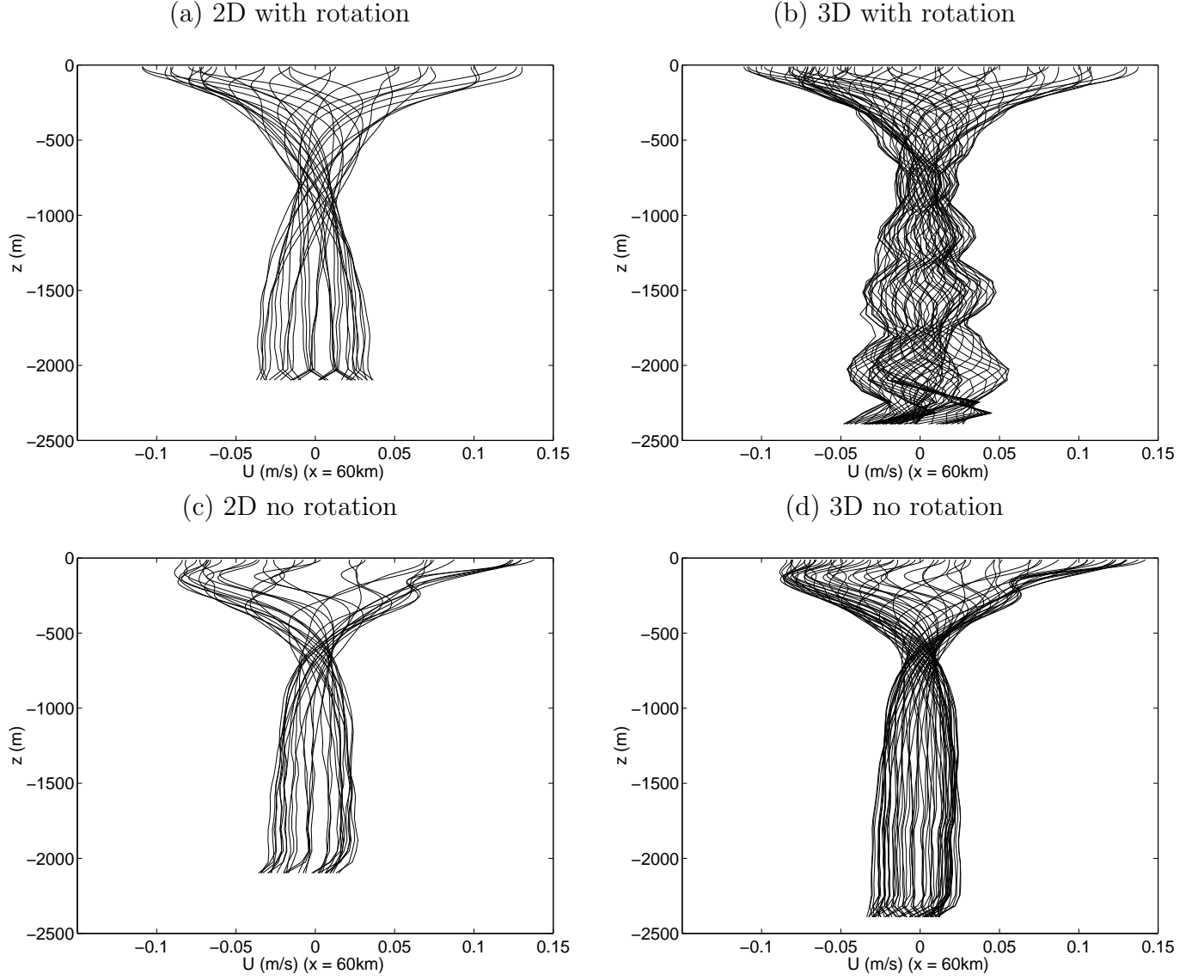


Figure 5: Vertical profiles of cross-slope baroclinic velocity at a location $x=58.7\text{km}$, $y=1.56\text{km}$ shown over several tidal cycles for (a) 2D calculation with the along-slope average topography, (b) 3D calculation with corrugated topography (c) 2D calculation with no rotation, (d) 3D calculations with corrugated topography, but without rotation.

Comparison with observed cross-slope velocity profiles (Nash et al, 2003, figure 8a) shows that the observed profiles can also be described as a combination of high and low modes, such that there are, as in the simulations, nodes of reduced variance and nodes of increased variance. In the observations, the small-vertical scales are found all the way up the water column, whereas in the simulations they are predominantly near the bottom, perhaps because the finite integration time doesn't allow them to propagate sufficiently high in the water column.

It seems likely that the structure in the cross-slope velocity field is a consequence of the reflection of the internal wave from the corrugated topography. To verify this hypothesis, we compare calculations with corrugations placed in three different locations - (a) onshore of the intersection of the characteristic with the bottom (i.e. in the shadow zone) (b) at the point of intersection and (c) offshore of the intersection. This is most easily achieved with a somewhat modified topography (figure 6). We have replaced the finite continental slope with a cliff, with the shelf break in the same location as before, with the corrugations placed on the flat bottom below the cliff in the three locations described above. In case (b) and (c) the high-mode structure is seen before, but in case (a), where the incident wave does not encounter the corrugations, there is little structure above the topography. In all these cases the extent of the corrugations in the x-direction is about 50km, much greater than their wavelength in the y-direction (3.33km). In cases (b) and (c) the high-mode structure is confined to the region above the topography, and does not appear to propagate either toward or away from the slope appreciably during the calculation period.

These calculations therefore demonstrate that the high-mode structure only results when the internal tide from the shelf-break encounters the corrugations: internal wave scattering at the corrugated topography is therefore the most likely source of the high-mode structure.

Now in figure 7 we examine the effect of increasing the wavelength of the corrugations. As the wavelength is increased, the number of nodes decreases until by $\lambda = 33.3km$, the structure has almost returned to the 1st mode form found without the corrugations. Hence we see that small-scale corrugations are needed to produce the variability on small vertical scales. Since we find similar features with and without the background slope (compare figure 7a and figure 5b) evidently the background slope is not essential for the generation of this small-scale structure (although there are certainly some quantitative differences).

3.3 Wave scattering and interference

Since it appears that the structure on small vertical scales results when the internal wave generated at the shelfbreak scatters from the corrugated slope, we compare our numerical results with analytic predictions derived by Thorpe (2001) for the reflection and scattering of internal waves from a slope with corrugations of the form $h = h_a \sin(Kx + Ly)$. Thorpe's original analysis is for nonrotating waves; in the appendix we have extended it to include rotation.

Thorpe considers the dependence of the reflection and scattering process on a large number of parameters, including the background slope of the topography α , the wavenumber of the incident wave $\mathbf{k} = (k, l, m)$ and the wavenumber of the topography $\mathbf{K} = (K, L)$. In all our simulations $l = 0$, and $K \ll L$ so that we will assume $K = 0$.

(a) Flat-bottomed case

Cross-slope velocity
 $t=3.14T$

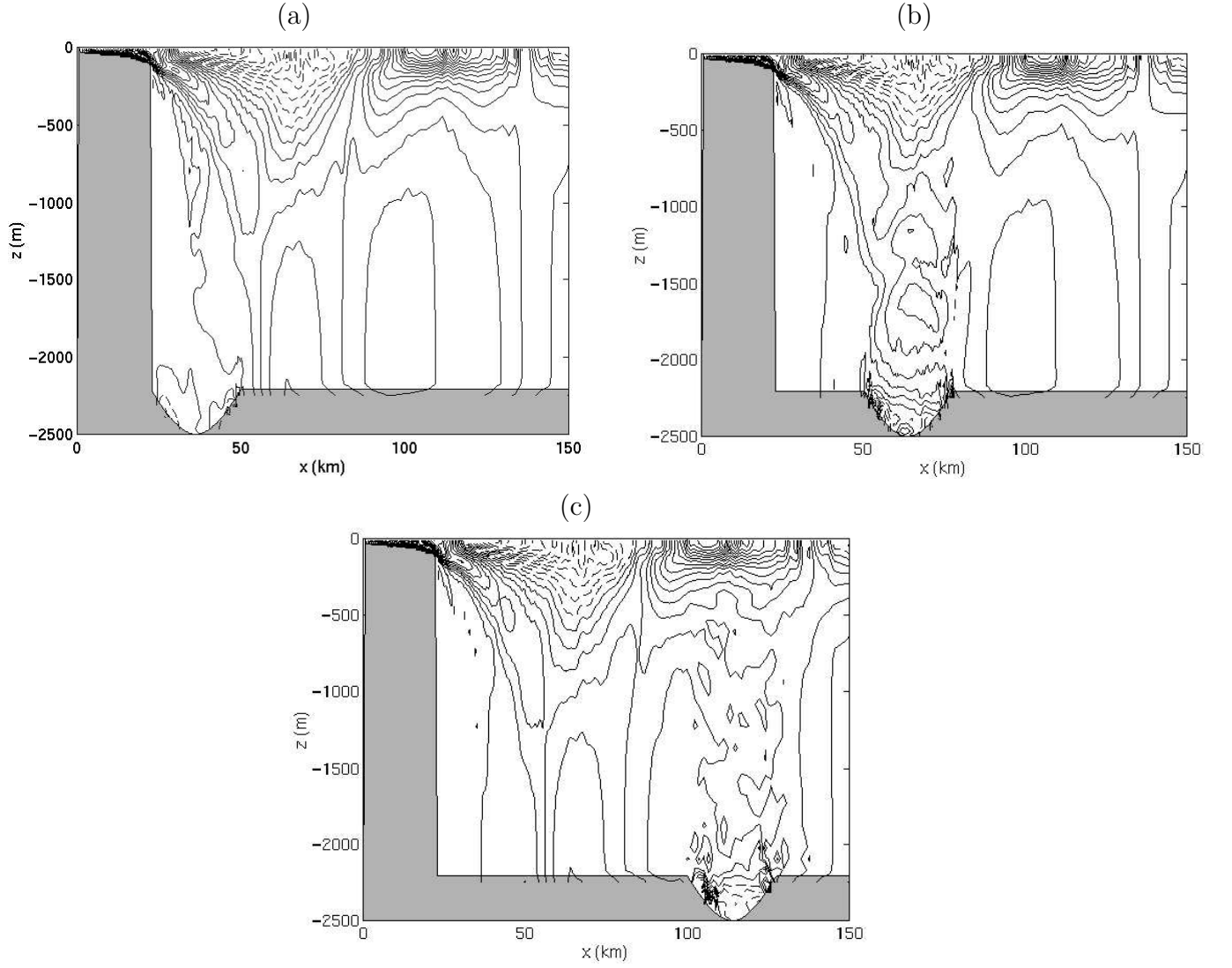


Figure 6: Snapshots of the cross-slope velocity field as shown in figure 3 but where the sloping topography has been replaced by a cliff, with corrugations placed at the bottom of the cliff. The corrugations are limited in horizontal extent, and placed (a) onshore of the intersection of the wave characteristic emanating from the shelf break with the bottom, - i.e. in the “shadow zone”, (b) at the point where the wave characteristic from the shelf break intersects the bottom (c) offshore of the intersection point.

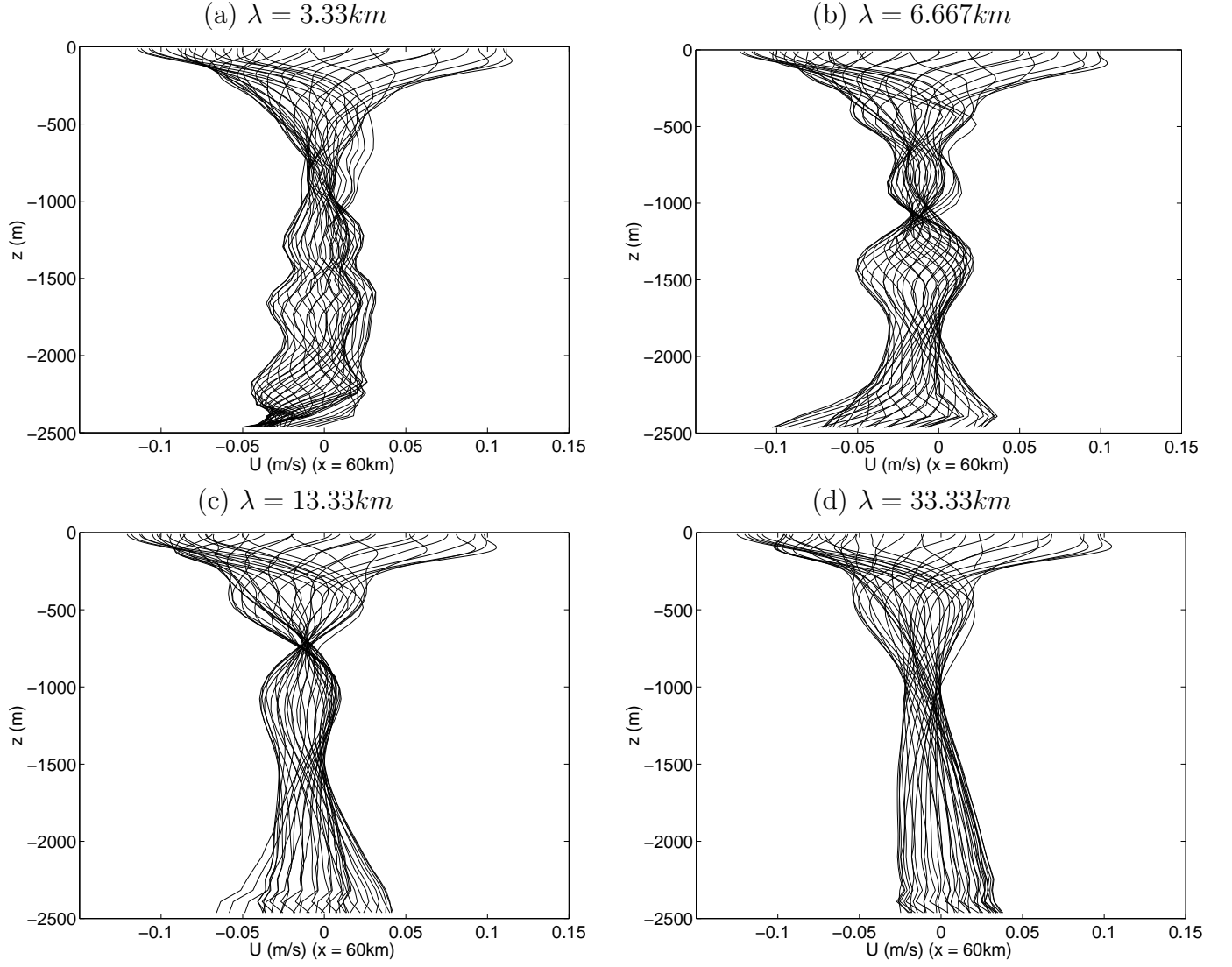


Figure 7: Vertical profiles of the cross-slope baroclinic velocity at a location $x=58.7\text{km}$, $y=1.56\text{km}$ shown over several tidal cycles for the cliff topography, with corrugations placed at $x=75\text{km}$ where the wave characteristic from the shelf break intersects the bottom. The wavelength of the corrugations varies from (a) $\lambda = 3.33\text{km}$, (b) $\lambda = 6.67\text{km}$, (c) $\lambda = 13.33\text{km}$, and (d) $\lambda = 33.33\text{km}$.

First we examine $\alpha = 0$, the flat-bottomed case, to highlight the role of the corrugations and rotation in generating high-vertical wavenumbers. The reflected waves consist of a primary wave with wavevector $\mathbf{k} = (k, 0, -m)$ and frequency equal to that of the incident wave, and scattered waves of the same frequency but different wavevectors: $\mathbf{K}_{\pm} = (k, \pm L, m_{\pm})$, where m_{\pm} satisfies the usual internal wave dispersion relation. In the absence of rotation, the predicted amplitudes of the scattered waves are

$$\frac{a_{\pm}}{a} = \pm h_a m \quad (7)$$

In our simulations we have $h_a = 300m$. Assuming the first vertical mode has wavelength $2H$ where $H = 2500m$, then $a_{\pm}/a = 0.37704$.

With rotation the scattered waves include an extra component with amplitude :

$$\frac{a_{\pm}}{a} = h_a m \frac{L}{k} \frac{f}{\omega} \quad (8)$$

which, for a corrugation wavelength of 3.33km, horizontal wavelength k calculated from the dispersion relation, m appropriate to the first mode, and $N = 5 \times 10^{-4} s^{-1}$ appropriate for the bottom, gives $a_{\pm}/a = 1.9354$. The ratio of nonrotating to rotating amplitudes is 5.13 for these parameters.

While this scattering theory does show that rotating waves can lead to more effective scattering than nonrotating waves on corrugations oriented parallel to the horizontal wavevector the full magnitude of this difference appears to be underestimated, since in the nonrotating simulations no evidence at all is seen for any scattered wave. Furthermore it should be recalled that the theory only strictly applies for small amplitude topography, and in our case R_h , the topographic steepness far exceeds 1.

Now we examine how the combination of incoming and scattered waves can lead to the structure seen in the cross-slope velocity profiles in the presence of rotation and topography (figure 5b). The cross slope velocity is given by the sum of the incoming wave, the primary reflected wave and the two scattered components. In figure 8 we show profiles for rotating internal waves, calculated assuming a constant stratification appropriate to the bottom: $N^2 = 2.4 \times 10^{-7} s^{-2}$, and incoming wave with $m = \pi/H$, and $H = 2500m$, $\omega = 1.4 \times 10^{-4} s^{-1}$, $h_a = 300m$, calculated at $x = 0$. The topographic wavenumber in the x-direction is $K = 2\pi/(125 \times 10^3)m^{-1}$, the length scale over which the corrugations are imposed, i.e. the length scale of the background slope (NB $K \ll k$). The topographic wavenumber in the y-direction L varies, and may be greater than k . Interference patterns similar to those found in the simulations are predicted, and the number of nodes decreases as the wavelength of the corrugations in the along-slope direction increases (decreasing L). Without rotation (figure 9) the profiles are modified only slightly from the first mode form expected without corrugations. We conclude that the structure found in the 3D simulations may be attributed to scattering on the corrugated topography, with rotation playing an important role in allowing corrugations oriented parallel to the plane of the wavevector to cause significant scattering.

From equation 8, the nondimensional parameter which determines the relative importance of scattering is L/k , the ratio of the horizontal wavenumbers of topography and of the wave. If the primary wave is a 1st mode wave, then $k = ms = \pi s/H$, so that $L/k = 2H/(\lambda s)$, where λ is the topographic wavelength, H is the depth of the fluid and s , the internal wave group velocity slope is given by equation 1. Scattered waves are only important for large L/k , i.e. large $H/(\lambda s)$.

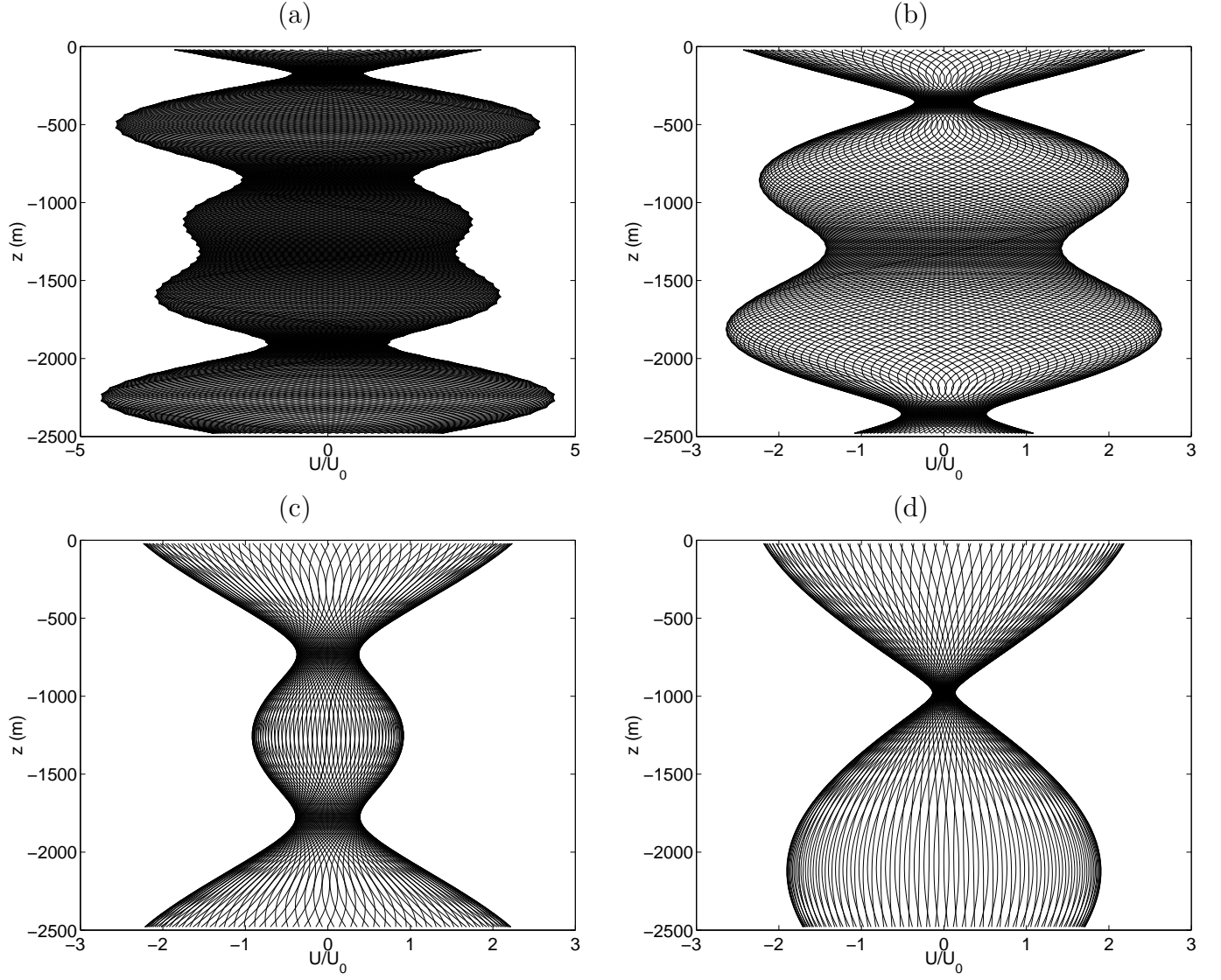


Figure 8: Cross-slope velocity profiles predicted from the combination of incident, reflected and scattered waves, assuming that the waves encounter topography with no mean slope, but with corrugations orientated in the direction of the wave vector. The profiles are calculated assuming a constant stratification $N^2 = 2.4 \times 10^{-7} s^{-2}$, incoming wave with vertical mode number $m = \pi/H$, and $H = 2500m$, $\omega = 1.4 \times 10^{-4} s^{-1}$. The topography has the form $h = h_a \sin(Kx + Ly)$ where $h_a = 300m$, $K = 2\pi/(125 \times 10^3)m^{-1}$ and $\lambda = 2\pi/L$ is (a) $3.33km$, (b) $6.667m$, (c) $13.33km$ and (d) $33.33km$.

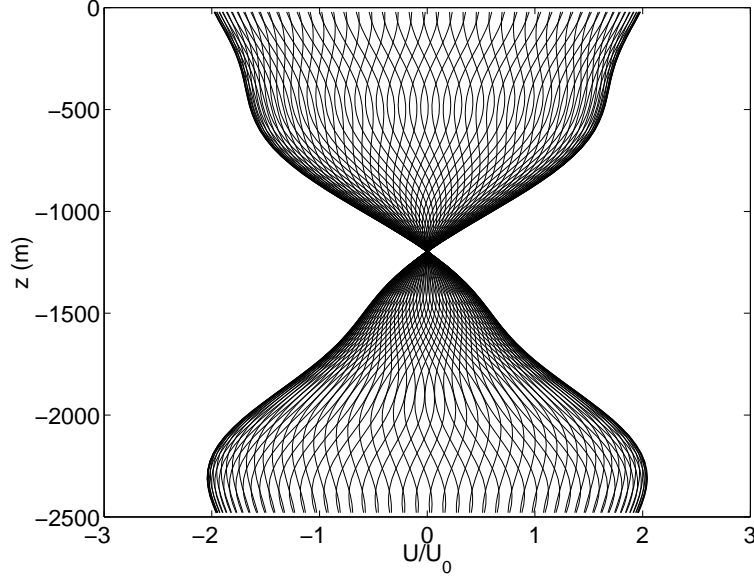


Figure 9: Cross-slope velocity profile for nonrotating flow, predicted from the combination of incident, reflected and scattered waves, assuming that the waves encounter topography with no mean slope, but with corrugations orientated in the direction of the wave vector. The profiles are calculated assuming a constant stratification $N^2 = 2.4 \times 10^{-7} s^{-2}$, incoming wave with vertical mode number $m = \pi/H$, and $H = 2500m$, $\omega = 1.4 \times 10^{-4} s^{-1}$. The topography has the form $h = h_a \sin(Kx + Ly)$ where $h_a = 300m$, $K = 2\pi/(125 \times 10^3)m^{-1}$ and $\lambda = 2\pi/L = 3.33km$

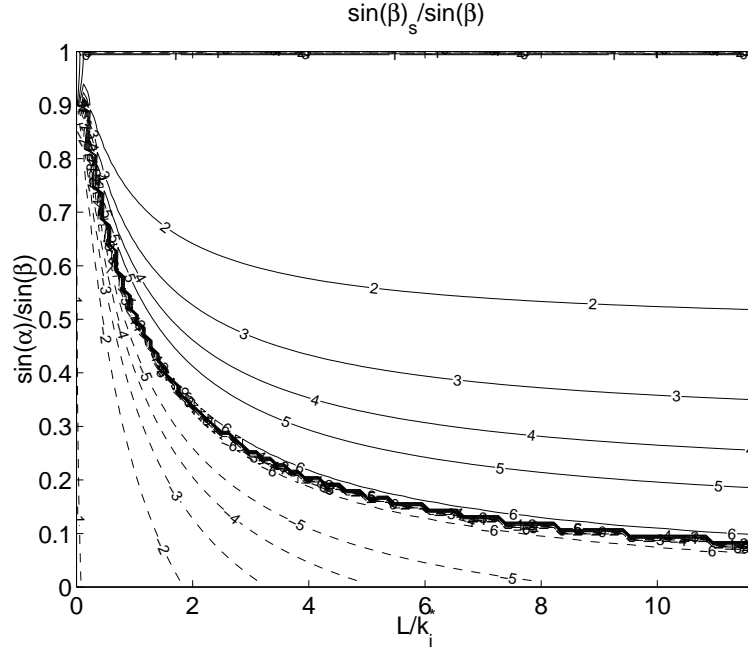


Figure 10: The angle between the scattered wave group velocity projected onto the (x,z) plane and the horizontal β_s as a function of slope angle α , and along-slope topographic wavenumber L , for the negative root. $\sin(\alpha)$ and $\sin(\beta)_s$ are normalized by $\sin(\beta)$, where β is the angle of incoming wave characteristic to the horizontal. L is normalized by the incoming cross-slope wavenumber k_i^* . Dashed contours indicate negative values.

(b) Finite slope

As shown in the appendix, the topographic slope modifies the amplitude of the scattered wave components slightly. More significant is the impact of the slope on the direction of the scattered wave. For large slopes and large L , the scattered wave may be directed back up the slope. The projection of the group velocity vector of the scattered wave onto the (x,z) plane has an angle β_s to the horizontal. The relationship between β_s and the slope angle α and corrugation wavenumber L is derived in the appendix.

In figure 10 the ratio of $\sin(\beta_s)/\sin(\beta)$ is shown as a function of $\sin(\alpha)/\sin(\beta)$ and L/k_i where β is the angle the internal wave characteristic makes to the horizontal, and k_i is the incident wave horizontal wavenumber. For small α and L , $\sin(\beta_s)$ is negative, corresponding to $k_s > 0$ and $m_s < 0$, (where k_s and m_s are the horizontal and vertical wavenumbers respectively of the scattered wave) and an offshore propagating scattered wave. For large α and L , $\beta_s > 0$, with $k_s < 0$ and $m_s < 0$, corresponding to an upslope propagating scattered wave.

In the sloping bottom 3D numerical calculation, the characteristic from the shelf break intersects the slope at a depth $d = 2029m$, where the slope gradient $dh/dx = 0.0308$. The stratification at this depth is $N^2 = 3.73 \times 10^{-7} s^{-2}$. Assuming a first mode structure for the incident wave with $m_i = \pi/d$ and $k_i = sm_i$, for corrugations with wavelength 3.33km we have $\sin\alpha/\sin\beta = ???$, and $L/k_i = ???$. Then from figure 10, the scattered wave has a group velocity vector projected into the

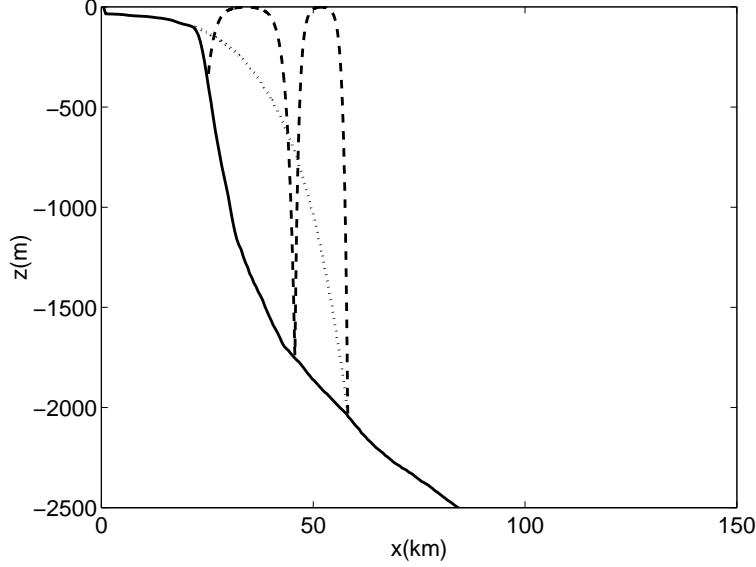


Figure 11: The mean slope in the (x,z) plane (solid), with the wave characteristic emanating from the shelf break (dotted) and the projection of the scattered wave characteristic onto the (x,z) plane (dashed) overlain.

(x,z) plane with a slope $\tan(\beta_s) = 2.32$, projected back up the slope. A plot of the scattered wave ray path (figure 11) shows that this scattered wave, by reflecting from the surface and the bottom boundary, could eventually reach into the "shadow zone" beneath the characteristic of the internal tide emanating from the shelfbreak. However, this would not occur within the timeframe of our simulations, so we cannot assess the possibility for this scattered wave to lead to mixing in the shadow zone.

As mentioned earlier, in the actual TWIST observation region, corrugations of wavelength $\sim 3km$ are more likely found higher up the slope than at 2000m depth. At that depth the dominant wavelength is around 25km. From eqn 43 corrugations of wavelength $> 5.46km$ will lead to offshore scattered waves, not upslope scattered waves. There is still the possibility that further scattering of the scattered wave could lead to more upslope propagating waves, when the first scattered wave hits topography at an oblique angle, but this would be outside the domain of our numerical calculations.

We summarize our comparison of numerical model results with theoretical predictions of wave scattering: (a) The wave scattering theory predicts much greater amplitude of scattered waves for nonzero coriolis for this particular topography configuration, as seen in the numerical calculations. (Note that if the incident waves were not propagating perpendicular to the shelf-break, or if the corrugations were orientated differently, a nonrotating wave would have a velocity component in the direction of the corrugations, and scattered waves could be generated without invoking rotation). (b) The wave scattering theory predicts larger vertical wavenumbers for the scattered waves as the wavelength of the corrugations decreases, as seen in the simulations. (c) The wave scattering theory predicts an upslope scattered wave, potentially leading to wave activity in the shadow zone, which we are unable to see in our short duration simulations.

There are many assumptions in the scattering theory which are not valid in the numerical model. As shown by Bell (1975), for large amplitude currents the waves generated at topography need not be confined to the forcing frequency, but can include higher harmonics. Similarly it is possible that the scattered waves need not be at the same frequency as the incident wave, but may include higher harmonics too. We intend to examine this further in future. In addition, as mentioned above, the steepness of the corrugated topography is expected to modify the spatial structure of the scattered wave (Baines, 1982; Balmforth et al, 2001; Khatiwala, 2001).

3.4 Instability and mixing

The 3D calculations described above show the emergence of higher vertical wavenumber structure in the velocity field. However, the shears involved are not sufficient to lead to instability and local mixing. If the forcing amplitude is increased, so that the Richardson number is decreased, instability is possible and mixing can occur in the valleys. An example of such mixing is shown in figure 12 for forcing amplitude $U_0 = 0.3m/s$. The shear in the valleys is sufficient that in this low stratification region $Ri < 1/4$, and Kelvin-Helmholtz instability results.

3.5 Internal tide energy flux

How do the corrugations affect the energy transferred from the barotropic tide to the internal tide? We examine this question by focusing on the internal wave horizontal energy flux in the cross slope (x) direction, defined as

$$\text{Energy flux} = p' u' \quad (9)$$

where p' is the internal wave perturbation pressure and u' is the baroclinic perturbation velocity. We define $u' = U - U_{bt}$ where U_{bt} is the barotropic velocity obtained from a barotropic calculation with identical forcing and topography, but only one model level and no stratification. We define p' through $\int_{n\lambda} p' dx = 0$ and $\int p' dz = 0$, to obtain the perturbation pressure which is associated with the internal wave only. Figure 13 shows the horizontal energy flux integrated over the whole water column as a function of time and horizontal distance for 3 different 2-dimensional calculations (Since these calculations are 2D they do not have corrugated topography) two calculations with $f = 10^{-4}s^{-1}$ but different amplitude tidal forcing, and one calculation with $f = 0$. High energy flux is initiated at the shelf break and propagates away from the slope. One interesting feature is that the energy flux appears to decay much more rapidly in the rotating experiments than in the nonrotating case. This cannot be attributed to the difference in interaction with the corrugated slope since there is no corrugated slope in these calculations. Instead it seems to be more that the rotating calculations take longer to reach a quasi-steady state, perhaps because the impulsive start to the forcing also generates inertial oscillations. In the nonrotating case, the first wavecrest retains sufficient energy when it reaches the offshore boundary for a large amplitude reflected wave to appear, a byproduct of the boundary conditions which are not radiative.

Now we compare 4 different rotating cases (figure 14), in a single snapshot of the vertically integrated energy flux at time $t = 2.87$ M2 tidal periods (before the energy flux signal has propagated out to the offshore boundary of the calculation). Two of the calculations are 2-dimensional,

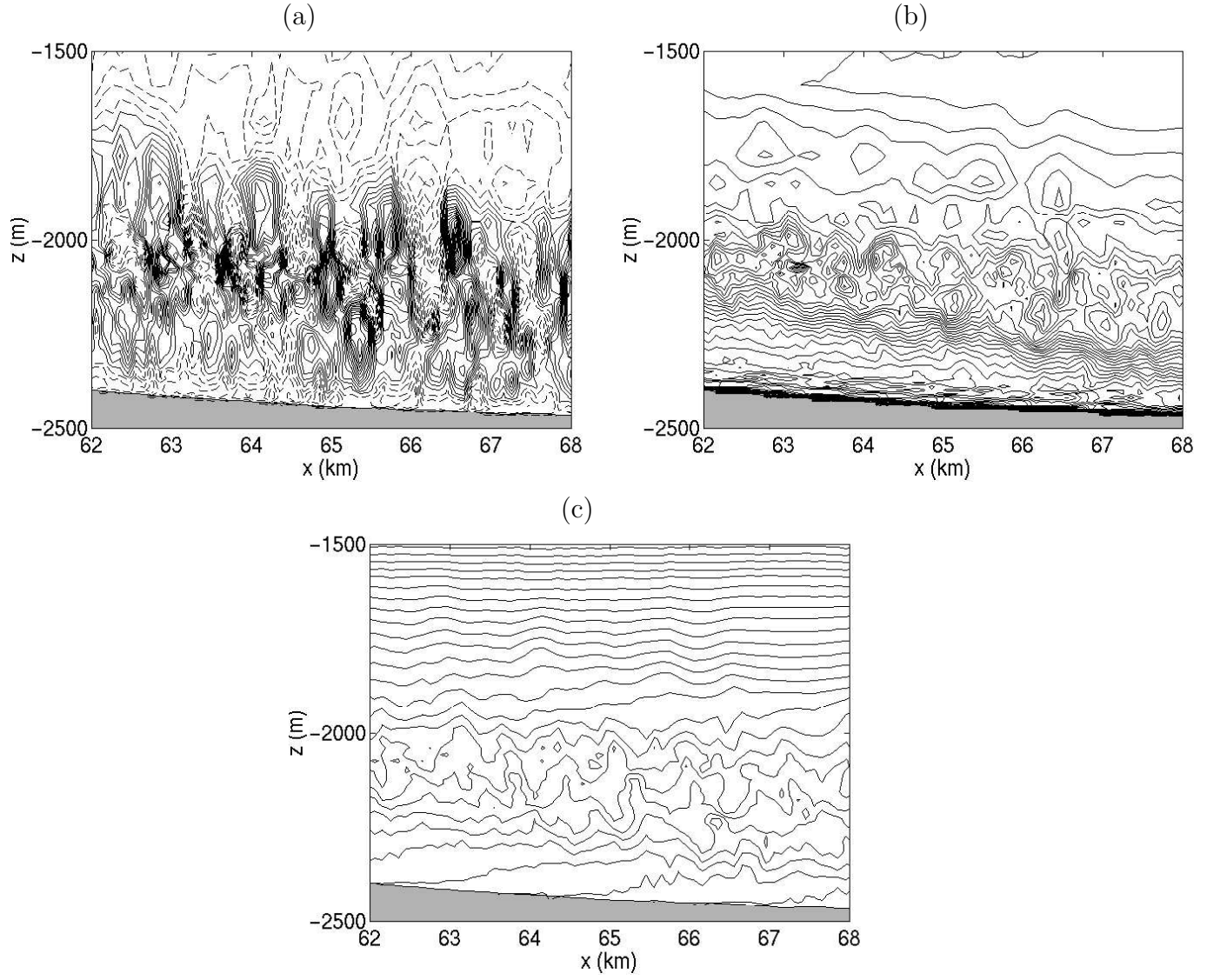


Figure 12: Fields from a 3D calculation with cross-slope barotropic forcing, with $U_0 = 0.3m/s$ at a location $y = 1.56km$ and time $t = 1.25T$; (a) vertical velocity (contour spacing = $0.002m/s$), (b) cross-slope velocity (contour spacing = $0.01m/s$), (c) temperature (contour spacing = $0.0075K$).

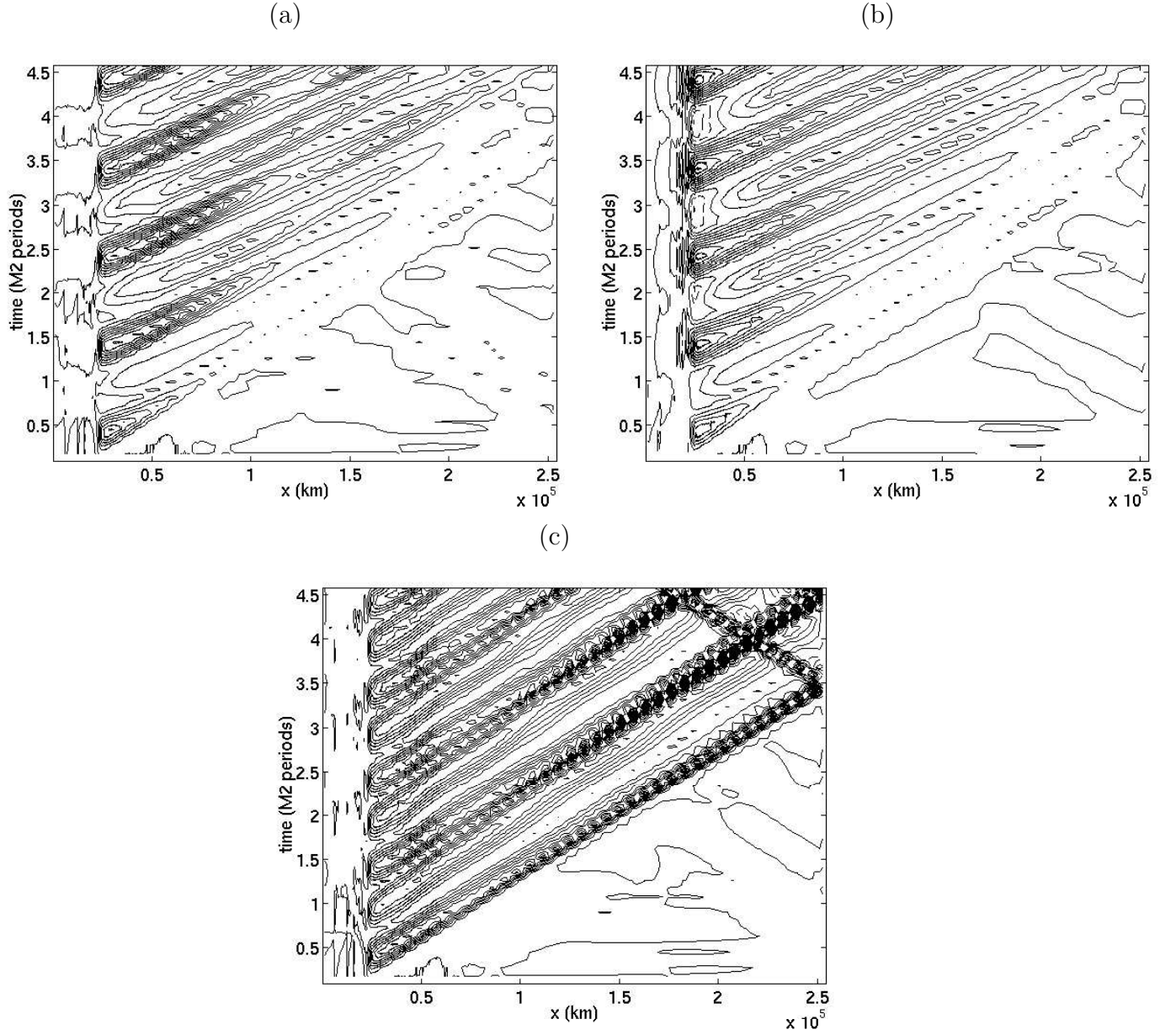


Figure 13: The vertically integrated horizontal energy flux $Ef = \int_h p' u' dz$ as a function of time and cross-slope distance in 2-dimensional calculations with no along-slope variations in topography for barotropic forcing of (a) $U_0 = 0.1 \text{ m/s}$, $f = 10^{-4} \text{ s}^{-1}$, contour spacing = 500 kgms^{-3} , (b) $U_0 = 0.02 \text{ m/s}$, $f = 10^{-4} \text{ s}^{-1}$, contour spacing = 25 kgms^{-3} and (c) $U_0 = 0.1 \text{ m/s}$, $f = 0$, contour spacing = 500 kgms^{-3} .

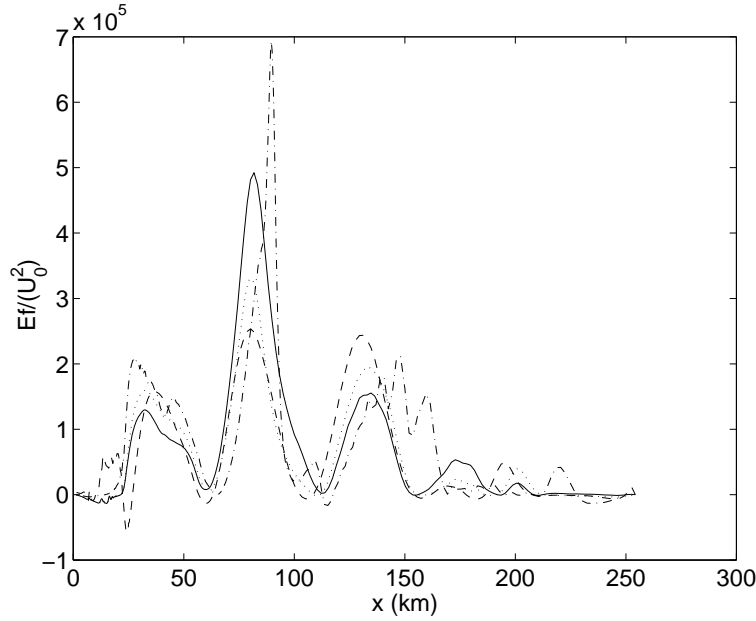


Figure 14: The vertically integrated energy flux, scaled by U_0^2 for $U_0 = 0.1m/s$, 2D (solid), $U_0 = 0.02m/s$, 2D (dashed), $U_0 = 0.1m/s$ 3D with corrugated topography (dotted), and $U_0 = 0.3m/s$ 3D with corrugated topography and mixing (dot-dash), at $t = 2.87T$ after the beginning of the calculation.

and correspond to the calculations described in figure (13) a and b. The other 2 calculations are 3-dimensional, including corrugated topography, one with $U_0 = 0.1m/s$ (corresponding to the calculation shown in figure 3). The other with $U_0 = 0.3m/s$ includes instability and mixing (corresponding to the calculation shown in figure 12). In all cases the energy flux is scaled by U_0^2 . We see little significant difference in the scaled energy flux between the 4 cases, suggesting that energy flux scales like U_0^2 as predicted by Baines (1982). Certainly there are some differences in the precise magnitude of the peaks, and their sharpness, but these may not be significant in a time-integral sense (although the short duration of our calculations does not allow us to determine this for certain). (The spatial structure seen in figure 3 is due to the instantaneous nature of the diagnostic. Each peak indicates a half-wavelength of the dominant mode internal tide). Perhaps surprisingly the addition of corrugations makes little difference to the energy flux, even when those corrugations lead to mixing (to see the influence of corrugations, the solid line and dotted line in figure 3 should be compared - both have forcing of $U_0 = 0.1m/s$, one without corrugations, one with corrugations.) A possible reason for the apparent insensitivity of the energy flux to the corrugations is that most of the energy flux signal is due to the strong density anomalies and velocities in the upper part of the water column, which is least affected by the topography and the mixing. Furthermore the energy flux is dominated by the largest scales, which are relatively unchanged by the scattering. Hence although we observe mixing in the large amplitude simulation ($U_0 = 0.3m/s$), the energy loss involved in this mixing is not a large fraction of the total energy flux. Time-averaged fluxes from a longer calculations would be needed to examine whether the mixing is balanced by the

divergence of the wave energy flux. By comparison, the observations show an energy flux which is orientated predominantly in the along-isobath direction, which is suggested by Nash et al (2003) to be a signature of superposed on and off-shore propagating waves.

4 Discussion and conclusions

We have shown, through a series of numerical calculations, that internal tides generated at the shelf-break by the cross-slope barotropic tide can lead to high vertical wavenumber structure in the velocity field when they reflect and scatter from corrugations oriented so that ridges and valleys run up and down the slope. This high wavenumber structure is absent if the Coriolis force is ignored. Linear scattering theory gives a qualitative agreement with the numerical simulations, showing that the smaller the wavelength of the corrugations, the more vertical structure is found in the velocity field, and emphasizing the importance of planetary rotation for this orientation of corrugations.

Comparison with the observations shows that similar high wavenumber structure is seen above the corrugations. However there are many differences between our results and the observations, as detailed in Nash et al (2003): (a) The high wave number structure is observed in the shadow zone below the characteristic emanating from the shelf break, whereas there is no baroclinic flow in the shadow zone in our simulations, with or without corrugations. (b) The observed energy flux is predominantly along-isobath, in contrast to the offshore energy flux in our simulations. Nash et al (2003) propose these two features can be explained by a low mode internal tide generated elsewhere and reflecting from the concave slope. They suggest that the Blake Escarpment might be the generation site for this incident low mode internal tide. The superposition of incident and reflected waves propagating in the on- and offshore directions respectively would lead to little net energy flux in the cross-slope direction. Nash et al (2003) suggest that the reflection from a near-critical slope could be the source of the high mode number structure. Nash et al (2003) discount the role of the corrugations, since they believe that corrugations on the wavelengths observed (2-3km) would generate structure with vertical lengthscales smaller than observed. However, our simulations indicate the scattered waves have wavelengths of the order of 300-500m, in agreement with the observed high-mode structure. In summary it seems likely that the interaction between locally generated internal tides and the topography does not explain the observations. Nonetheless, the process of wave reflection from corrugated topography may still be important in generating high-mode number scattered waves when a remotely generated wave encounters the slope, both at this location and other corrugated slopes around the globe. For many steep/concave continental slopes, internal tides might also be generated locally at the shelf-break as in these simulations. The relative importance of locally versus remotely generated waves will vary from location to location, depending on factors such as the proximity of other generation sites, and the orientation and magnitude of tidal ellipses.

Another source of mixing in a region of corrugated slope is the along-slope component of the barotropic tide, which we have ignored here - a second paper (Legg, 2002) examines the response of the flow to along-slope barotropic forcing. However, that study indicates that strong mixing would only be found for along-slope flow speeds larger than observed in the TWIST region.

We have not attempted to quantify the mixing produced by the scattering of internal tides

from topography. The magnitude and spatial distribution of mixing would depend on the location of dissipation of the small-scale waves once an equilibrium is reached. For example high mode-number waves take longer than the current calculation to propagate into the shadow zone. This model configuration cannot be run to equilibrium since the internal waves eventually reflect from the offshore boundary. Instead we have focused on the conditions under which small-scale shear is produced, since such shear is a pre-requisite for mixing.

In conclusion, we have shown that cross-slope barotropic tide leads to an internal tide generated at the shelf break. This internal tide takes the form of the lowest vertical mode after reflection from the bottom, in the absence of topographic variations. When topographic corrugations are included in the presence of planetary rotation, higher wavenumber structure is found above the topography, which if the forcing is sufficiently large (in our simulations $\geq 0.3m/s$, larger than seen in the observations) can provide sufficient shear to lead to mixing. More vertical structure is found as the wavelength of the corrugations is decreased. A linear scattering model for internal wave interaction with corrugated topography, based on that of Thorpe (2001) but extended to include rotation, agrees qualitatively with the behavior of the numerical simulations, describing the influence of rotation and topographic wavenumber on the net velocity profiles. The principal influence of rotation on internal waves is to add a velocity component in the direction perpendicular to the plane of wave propagation, pushing fluid up and over topographic variations in that direction. Hence rotation provides 1st order modifications to the interaction of internal waves with complex topography.

In terms of the nondimensional parameters listed in the introduction, we have examined a regime in which the tidal excursion is small compared to the topographic variations in the direction of the tidal flow ($R_L \ll 1$), but topography is steep relative to the internal tide characteristic slope ($\epsilon > 1$). Such scenarios would be typical of many continental slopes, and abrupt ridges such as Hawaii. In the absence of topographic variations in the along-slope direction, this scenario leads to low mode internal tides, and little possibility for local mixing. However, the addition of topographic variations in the alongslope direction can scatter incident low mode internal tides into higher modes, with greater associated shear (especially at depth), more likely to lead to mixing. Importantly, smaller vertical length scales are only present in the scattered wave if the corrugation lengthscale is sufficiently small i.e. $\lambda < H/s$ (where s is the wave characteristic slope). Therefore we can say that in general corrugated continental slopes with $H/(\lambda s) > 1$ are locations where scattering of low modes might lead to conditions more suitable for mixing (whether or not mixing occurs will of course depend on the amplitude of the wave, the amplitude of the corrugations, and the stratification).

Acknowledgments

This work has been funded by ONR grant N00014-98-1-0096, with calculations carried out on NRL supercomputers. I am grateful to Kurt Polzin for the substantial role he has played in the development of this manuscript. Discussions with Jonathan Nash, Samar Khatiwala and Carl Wunsch have all aided in the course of this study.

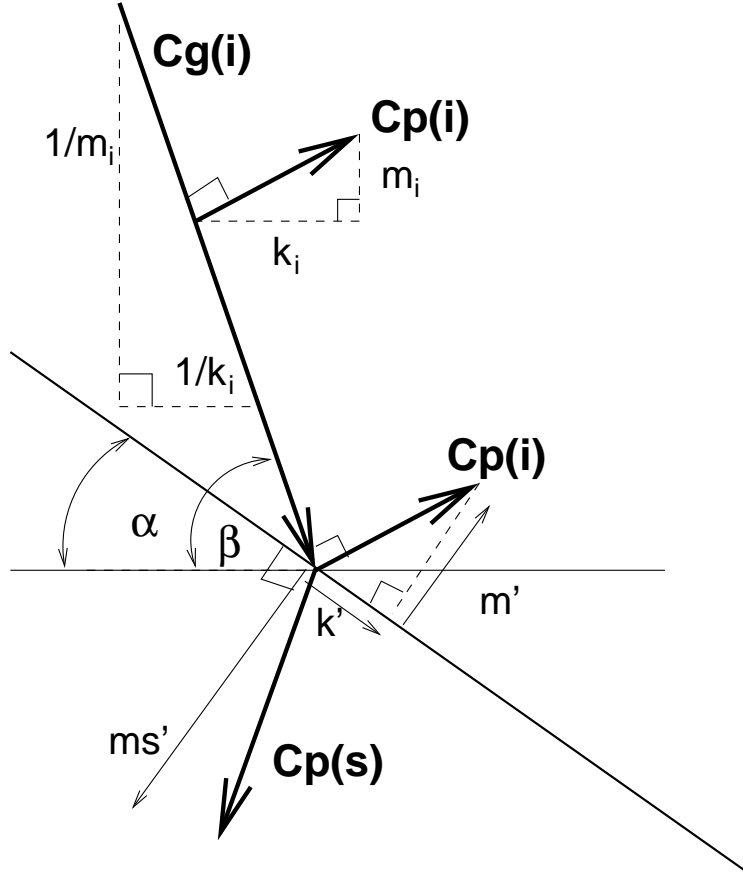


Figure 15: A schematic diagram showing the group velocity vector \mathbf{C}_g and phase velocity vector \mathbf{C}_p of the incident wave in the (x, z) plane, where the group velocity is at an angle β to the horizontal. The wave scatters off a slope at angle α to the horizontal. The scattered wave has wave vector components (k', L, m'_s) in the coordinate system aligned with the slope, where L is the along slope topographic wave number.

Appendix: Wave scattering at corrugated sloping topography including Coriolis effects

Thorpe (2001) describes the reflection and scattering of nonrotating internal waves from a sloping corrugated boundary. Here we extend his theory to include rotation. (We note that Muller and Xu (1992) include rotation in their description of wave scattering from irregular topography: we prefer to use Thorpe (2001) as a starting point so as to highlight the effects of the mean bottom slope combined with the corrugations).

The full problem includes a large number of parameters: the angle of the background slope α , the angle of orientation of the corrugations relative to the slope β_C , the wavenumber of the incoming wave $\mathbf{k} = (k, l, m)$, the wavenumbers of the topography $\mathbf{K} = (K, L)$ and the amplitude of the topography and wave respectively h_a and a , as well as the frequency of the incoming wave

ω and Brunt-Vaisala frequency N . The maximum topographic slope is assumed to be aligned with the (x, z) plane. For simplicity we will assume an incoming wave traveling in the (x, z) plane: $l = 0$ (see figure 15) and explore the modifications to the scattering process introduced by nonzero Coriolis force. Thorpe's theory assumes that the incoming, reflected and scattered waves all have the same frequency ω (i.e. the intrinsic frequency of the flow U/L is ignored) and the steepness of the corrugations is assumed to be small.

The wave reflection/scattering is most easily understood in a coordinate system aligned with the slope. We therefore define rotated coordinates (x', z') (pointing down the slope, and normal to the slope respectively) which are related to the regular coordinates (x, z) by

$$x' = x \cos \alpha - z \sin \alpha \quad (10)$$

$$z' = x \sin \alpha + z \cos \alpha \quad (11)$$

(Note that our coordinate x' is aligned to point down the slope, (figure 15) whereas in Thorpe (1997, 2001) the slope aligned coordinate points up the slope. We make this change since our incident wave is coming from the upslope direction.)

In regular vertically aligned coordinates the incoming wave is of the form

$$U_I = \frac{a\omega}{s} \cos(kx + mz - \omega t) \quad (12)$$

$$W_I = -a\omega \cos(kx + mz - \omega t) \quad (13)$$

(as in Thorpe 2001) while V_I is given from the coriolis force:

$$\frac{\partial V_I}{\partial t} = -f U_I \quad (14)$$

$$V_I = \frac{f}{\omega} \frac{a\omega}{s} \sin(kx + mz - \omega t) \quad (15)$$

a is the amplitude of isopycnal displacements (units of height) and $s = k/m = \sqrt{((\omega^2 - f^2)/(N^2 - \omega^2))} = \tan(\beta)$, where β is the angle the group velocity vector makes with the horizontal.

Now in rotated coordinates the incoming wave flow is given by

$$U'_I = \frac{a\omega}{s} \left(\frac{c_\alpha c_\beta + s_\alpha s_\beta}{c_\beta} \right) \cos(kx + mz - \omega t) \quad (16)$$

$$W'_I = -a\omega \left(\frac{s_\alpha c_\beta - c_\alpha s_\beta}{s_\beta} \right) \cos(kx + mz - \omega t) \quad (17)$$

$$V'_I = V_I \quad (18)$$

and the wavenumber is $\mathbf{k}_I = (k', 0, m')$.

The primary reflected wave satisfies the boundary condition that $W'_I + W'_R = 0$ at $z = 0$, and has wave number $\mathbf{k}_R = (k'_R, 0, m'_R)$, where $k'_R = k'$ and m'_R is given by

$$m'_R = \left(\frac{s_\alpha c_\alpha - s_\beta c_\beta}{s_\beta^2 - s_\alpha^2} \right) k' \quad (19)$$

(from Thorpe, 1997). If $\alpha = 0$ then $m_R = -m_I$.

Then

$$U'_R = \frac{a\omega}{s} \frac{m'_R}{k'} \left(\frac{s_\alpha c_\beta - s_\beta c_\alpha}{c_\beta} \right) \cos(k'x' + m'_R z' - \omega t) \quad (20)$$

$$W'_R = a\omega \left(\frac{s_\alpha c_\beta - c_\alpha s_\beta}{s_\beta} \right) \cos(k'x' + m'_R z' - \omega t) \quad (21)$$

$$V'_R = \frac{f}{\omega} \frac{a\omega}{s} \left(\frac{(s_\alpha c_\beta - c_\alpha s_\beta)[s_\beta(c_\alpha c_\beta + s_\alpha s_\beta) - s_\alpha]}{c_\beta(s_\alpha^2 - s_\beta^2)} \right) \sin(k'x' + m'_R z' - \omega t) \quad (22)$$

The scattered wave amplitudes are found from the condition of zero flow normal to the rigid boundary:

$$u' \frac{\partial h'}{\partial x'} + v' \frac{\partial h'}{\partial y'} = w' \quad (23)$$

(applied in slope coordinates) at $h' = h_a \sin(Kx' + Ly)$, which at order aS (S is the steepness of the topography, $S = h_a(K^2 + L^2)^{1/2}$) becomes (from Thorpe 2001)

$$h_a \cos(Kx' + Ly)[K(U'_I + U'_R) + L(V'_I + V'_R)] = h_a \sin(Kx' + Ly) \left[\frac{\partial W'_I}{\partial z'} + \frac{\partial W'_R}{\partial z'} \right] + w'_+ + w'_- \quad (24)$$

evaluated at $z' = 0$, where w'_\pm are the forward and backward scattered wave velocities in the direction normal to the slope. Note that equation 24 is only strictly valid for small aS , i.e. small amplitude waves and topography.

Substituting for the incoming and reflected wave velocity components, we obtain the scattered wave velocities normal to the slope, at $z = 0$:

$$w'_\pm = h_a a \omega \left[\left(\frac{K}{s} \gamma_1 \mp m'_I \gamma_2 \right) \cos[(k' \pm K)x' \pm Ly - \omega t] + \frac{L}{s} \frac{f}{\omega} \gamma_3 \sin[(k' \pm K)x' \pm Ly - \omega t] \right] \quad (25)$$

where γ_1 , γ_2 and γ_3 are coefficients depending on the slope α , and equal to 1 if $\alpha = 0$:

$$\gamma_1 = \frac{s_\beta [s_\alpha c_\beta - c_\alpha s_\beta]}{s_\alpha^2 - s_\beta^2} \quad (26)$$

$$\gamma_2 = \frac{(s_\alpha c_\beta - c_\alpha s_\beta)^2 c_\beta}{(s_\alpha^2 - s_\beta^2)(s_\alpha s_\beta + c_\alpha c_\beta)} \quad (27)$$

$$\gamma_3 = \frac{s_\beta (s_\alpha c_\alpha - s_\beta c_\beta)}{c_\beta (s_\alpha^2 - s_\beta^2)} \quad (28)$$

To clarify the differences introduced by rotation, we focus now on the case of no bottom slope ($\alpha = 0, \gamma_1 = \gamma_2 = \gamma_3 = 1$). In the nonrotating limit, the amplitude of the scattered waves $a_\pm = w_{\pm 0}/\omega$ is given by

$$\frac{a_\pm}{h_a a m} = \frac{K}{k} \mp 1 \quad (29)$$

If $K = 0$ (i.e. no corrugations in the x direction) then $a_+ = -a_-$, and at $z = 0$, $w_+ = -w_-$.

When $f \neq 0$, but $K = 0$, then in addition to the cosine scattered component with amplitude as in equation 29 there is a sine component of amplitude

$$\frac{a_{f\pm}}{h_a a m} = \frac{L}{k} \frac{f}{\omega} \quad (30)$$

Note that for the rotating case, the scattered wave amplitude can be large ($a_{f\pm}/h_a a m \gg 1$) for topographic corrugations orientated both parallel to the direction of wave propagation (i.e. $K = 0$, $L \neq 0$) and corrugations perpendicular to the direction of wave propagation ($K \neq 0$, $L = 0$), whereas with nonrotating waves, large scattering only occurs if the topographic variations have a component direction of propagation ($K \neq 0$). Physically one can see that the reason for this difference is that the rotating wave has nonzero velocity in the direction perpendicular to the plane of wave propagation (i.e. $v \neq 0$), so that the fluid is forced over the topographic variations in that direction. We note that it is not really a surprize that rotation allows scattering from corrugations aligned with the plane of the incoming wave vector - it is simply a consequence of the fact that it is not possible for the wave velocity to be always normal to ∇h when $f \neq 0$. Without rotation, \mathbf{U} may be normal to ∇h for the special case of corrugations aligned with the plane of the incoming wave.

The horizontal velocities of the scattered waves can be found from

$$\frac{\partial \zeta}{\partial t} = -f \frac{\partial w}{\partial z} \quad (31)$$

and

$$-\frac{\partial \zeta}{\partial y} - \frac{\partial}{\partial x} \frac{\partial w}{\partial z} = \nabla_H^2 u \quad (32)$$

$$\frac{\partial \zeta}{\partial x} - \frac{\partial}{\partial y} \frac{\partial w}{\partial z} = \nabla_H^2 v \quad (33)$$

where $\zeta = \partial v / \partial x - \partial u / \partial y$, the vertical component of vorticity. Then

$$u_{\pm} = \frac{a h_a m_{\pm}}{((k \pm K)^2 + L^2)} \left[\left(\pm \frac{f^2 L^2}{s \omega} \pm \omega m k \right) \cos((k \pm K)x \pm Ly + m_{\pm}z - \omega t) \right. \quad (34)$$

$$\left. + \left(f L m - \frac{L f (k \pm K)}{s} \right) \sin((k \pm K)x \pm Ly + m_{\pm}z - \omega t) \right] \quad (35)$$

Now we reintroduce the background slope α . In addition to modifying the amplitude of the scattered wave (as in equation 25), the background slope changes the direction of the scattered wave, so that the group velocity of the scattered wave may actually be directed back up the slope under certain conditions.

If the corrugations are aligned up and down the slope, ($K = 0$), the wave number of the scattered wave in slope coordinates is $\mathbf{K}_s = (k', \pm L, m'_s)$ where

$$k' = k \cos \alpha - m \sin \alpha \quad (36)$$

(as for the incident and primary reflected wave) and

$$m'_s = \frac{k'c_\alpha s_\alpha - c_\beta \sqrt{k'^2 s_\beta^2 + (s_\beta^2 - s_\alpha^2)L^2}}{(s_\beta^2 - s_\alpha^2)} \quad (37)$$

(as in Thorpe (2001), given that $m^2/(k^2 + L^2 + m^2) = c_\beta^2$). Rotating back into coordinates aligned with the vertical and horizontal the scattered wave number is $\mathbf{K}_s = (k_s, \pm L, m_s)$ where

$$k_s = k' \cos \alpha + m'_s \sin \alpha \quad (38)$$

and

$$m_s = m'_s \cos \alpha - k' \sin \alpha \quad (39)$$

An incident wave with $k > 0$ may lead to a scattered wave with $k_s < 0$, so that energy propagates back up the slope. The phase velocity vector lies in a vertical plane which intersects the (x, z) plane at an angle θ where

$$\cos(\theta) = \frac{k_s}{(k_s^2 + L^2)^{1/2}} \quad (40)$$

The group velocity vector \mathbf{Cg}_s lies in the same vertical plane, and is at right angles to the phase velocity vector \mathbf{K}_s . The projection of the horizontal component of the group velocity onto the (x, z) plane is therefore

$$\frac{1}{X} = \frac{1}{\sqrt{(k_s^2 + L^2)}} \cos \theta = \frac{k_s}{(k_s^2 + L^2)} \quad (41)$$

and the angle the projection of the group velocity onto the (x, z) plane makes with the horizontal is

$$\tan(\beta_s) = \frac{X}{m_s} = \frac{k_s^2 + L^2}{m_s k_s} = \frac{(k' \cos \alpha + m'_s \sin \alpha)^2 + L^2}{(m'_s \cos \alpha - k' \sin \alpha)(k' \cos \alpha + m'_s \sin \alpha)} \quad (42)$$

Backscatter ($\tan \beta_s > 0$, with $k_s < 0$) occurs if the wavenumber L of the topographic corrugations is large enough, i.e.

$$\frac{L^2}{k'^2} > \frac{s_\beta^2(c_\alpha^2 s_\beta^2 - c_\beta^2 s_\alpha^2)}{c_\beta^2 s_\alpha^2 (s_\beta^2 - s_\alpha^2)} \quad (43)$$

For large L ($L \gg k$) we find that

$$\tan(\beta)_s = \tan(\beta) \frac{\tan(\beta)}{\tan(\alpha)} \quad (44)$$

Only the backward scattered solution $m_s < 0, k_s < 0$ is physically realisable in this case, since $\beta_s > \alpha$ (because $\beta > \alpha$). Hence for large L , the scattered wave energy is directed back up the slope. We remind the reader that this backscattered wave will only have significant amplitude for non-zero Coriolis.

The backscattered wave will reflect from the top surface, preserving the magnitude and direction of the horizontal components of the wavevector (k_s and L), and reversing the sign of the vertical

component of the wavevector ($m = -m_s$). Further reflections from the slope may occur. The wavenumber in the directions aligned down the slope ($k' = k_s \cos \alpha + m_s \sin \alpha$), and along the isobaths (L) are unchanged on reflection, but the wavenumber in the direction normal to the slope is changed, according to equation 37, for subcritical slope. As a result, after reflection, the wavenumber in the x-direction is increased in magnitude, while that in the y-direction is unchanged. The backscattered wave tends to travel more directly toward the shelf-break after every subsequent reflection from the slope (as described in Thorpe, 1996).

References

- Adcroft, A., C. Hill and J. Marshall, 1997: Representation of topography by shaved cells in a height coordinate ocean model. *Mon. Wea. Rev.*, **125**, 2293.
- Baines, P.G., 1982: On internal tide generation models. *Deep Sea Res.*, **29**, 307-338.
- Balmforth N.J., G.R. Ierley, W.R. Young, 2002: Tidal conversion by nearly critical topography. Submitted to *J. Phys. Oceanogr.*
- Bell, T.H. 1975: Topographically generated internal waves in the open ocean. *J. Geophys. Res.*, **80**, 320-327.
- Cox, C. and H. Sandstrom, 1962: Coupling of internal and surface waves in water of variable depth. *J. Oceanogr. Soc. Japan*, **18**, 499-513.
- Holloway, P.E., 2001: A regional model of the semidiurnal internal tide on the Australian North West Shelf. *J. Geophys. Res.*, **106**, 19625-19638.
- Khatiwala, S. 2002: Generation of internal waves in the ocean, submitted to *Deep Sea Res.*
- Ledwell J.L., E.T. Montgomery, K.L. Polzin, L.C. St Laurent, R.W. Schmitt and J. Toole, 2000: Evidence for enhanced mixing over rough topography in the abyssal ocean. *Nature*, **403**, 179-182.
- Legg, S., 2002: Internal tides generated on a corrugated continental slope: Part 2. Along-slope barotropic forcing. *J. Phys. Oceanogr.*, submitted.
- Marshall, J., A. Adcroft, C. Hill, L. Perelman, and C. Heisey, 1997. A finite-volume, incompressible Navier Stokes model for studies of the ocean on parallel computers. *J. Geophys. Res.*, **102**, 5753.
- Merrifield M.A., and P.E. Holloway, 2002: Model estimates of M-2 internal tide energetics at the Hawaiian Ridge. *J. Geophys. Res.*, **107**, article no 3179.
- Muller, P., and X. Liu, 2000a: Scattering of internal waves at finite topography in two dimensions. Part I: Theory and case studies. *J. Phys. Oceanogr.*, **30**, 532-549.

- Muller, P., and X. Liu, 2000b: Scattering of internal waves at finite topography in two dimensions. Part II: Spectral calculations and boundary mixing. *J. Phys. Oceanogr.*, **30**, 550-563.
- Muller P, and N. Xu, 1992: Scattering of oceanic internal gravity waves off random bottom topography. *J. Phys. Oceanogr.*, **22**, 474-488.
- Munk, W., and C. Wunsch, 1998. Abyssal recipes – II: energetics of tidal and wind mixing. *Deep Sea Res.*, **45**, 1977–2010.
- Nash, J.D., E. Kunze, J.M. Toole, R.W.Schmitt, 2003: Internal tide reflection and turbulent mixing on the continental slope. *J. Phys. Oceanogr.*, submitted.
- Polzin, K.L., J.M. Toole, J.R. Ledwell, and R.W. Schmitt, 1997: Spatial variability of turbulent mixing in the abyssal ocean. *Science*, **276**, 93-96.
- Polzin, K.L., 2002: Idealized solutions for the energy balance of the finescale internal wavefield. *J. Phys. Oceanogr.*, submitted.
- Rattray, M., 1960: On the coastal generation of internal tides. *Tellus*, **12**, 54-61.
- St Laurent, L.C., J.M. Toole, and R.W. Schmitt, 2001: Buoyancy forcing by turbulence above rough topography in the abyssal Brazil Basin. *J. Phys. Oceanogr.*, **31**, 3476-3495.
- St Laurent L., and C. Garrett, 2002: The role of internal tides in mixing the deep ocean. Submitted to *J. Phys. Oceanogr.*
- St Laurent, L., S. Stringer, and Chris Garrett, 2002: The generation of internal tides at abrupt topography. submitted to *Deep Sea Res.*
- Thorpe, 1992: The generation of internal waves by flow over the rough topography of a continental slope. *Proc. Roy. Soc. London, Ser. A*, **439** 115-130.
- Thorpe, S.A., 1996: The cross-slope transport of momentum by internal waves generated by alongslope currents over topography. *J. Phys. Oceanogr.*, **26**, 191-204.
- Thorpe, S.A., 2001: Internal wave reflection and scatter from sloping rough topography. *J. Phys. Oceanogr.*, **31**, 537-553.